

Self-assembled network polymer electrolyte membranes for application in fuel cells at 250 \times

Seungju Lee

Korea Institute of Science and Technology

YoungSuk Jo

Korea Institute of Science and Technology

Son-Jong Hwang

California Institute of Technology

Yongha Park

Korea Institute of Science and Technology

Yeong Cheon Kim

Korea Institute of Science and Technology

Tae Kyung Lee

Korea Institute of Science and Technology

Hyoung-Juhn Kim

Korea Institute of Science and Technology

Suk Woo Nam

Korea Institute of Science and Technology

So Young Lee (✉ sylee5406@kist.re.kr)

Korea Institute of Science and Technology <https://orcid.org/0000-0002-2003-5732>

Article

Keywords: energy storage, energy conversion devices, polymer electrolyte membrane, fuel cells

Posted Date: September 7th, 2021

DOI: <https://doi.org/10.21203/rs.3.rs-829052/v1>

License:   This work is licensed under a Creative Commons Attribution 4.0 International License.

[Read Full License](#)

1 Self-assembled network polymer electrolyte membranes
2 for application in fuel cells at 250 °C

3 Seungju Lee^{1,†}, YoungSuk Jo^{1,†}, Son-Jong Hwang², Yongha Park¹, Yeong Cheon Kim¹, Tae
4 Kyung Lee¹, Hyoung-Juhn Kim^{1*}, Suk-Woo Nam,^{1*} and So Young Lee^{1*}

5
6 ¹ Hydrogen Fuel Cell Research Center, Korea Institute of Science and Technology, 5,
7 Hwarangro 14-gil, Seongbuk-gu, Seoul 02792, Republic of Korea

8 ² Division of Chemistry and Chemical Engineering, California Institute of Technology,
9 Pasadena, California 91125, USA

10

11 *Corresponding authors:

12 S. Y. Lee (Email: sylee5406@kist.re.kr)

13 S. W. Nam (Email: swn@kist.re.kr)

14 H. -J. Kim (Email: hjkim25@kist.re.kr)

15

16

17

18

19

20

21

22 **Modern H₂-based energy storage and conversion devices require a polymer electrolyte**
23 **membrane (PEM) fuel cell-based integrated power system with synergistic heat**
24 **integration. The key issue in integrated power systems is developing a PEM that can**
25 **operate at 200–300 °C. However, currently used phosphoric-acid-based high-temperature**
26 **PEM fuel cells limited stability at higher operating temperatures. Herein, we introduce a**
27 **cerium hydrogen phosphate (CeHP) PEM that conducts protons above 200 °C through a**
28 **self-assembled network (SAN). The SAN-CeHP-PBI reached maximum power densities**
29 **of 2.4 W cm⁻² and operate stably for over 7000 minute without any voltage decay at 250 °C**
30 **under H₂/O₂ and anhydrous conditions. The developed fuel cell can be combined with an**
31 **external hydrogen generator that uses a liquid hydrogen carrier such as N-ethylcarbazole**
32 **and methanol as fuel, thus achieving a high energy efficiency. The thermal stability and**
33 **fuel flexibility of these SAN-CeHP-PBI demonstrate potential for commercial**
34 **applications.**

35
36
37
38
39
40
41
42
43
44

45 Climate change and growing environmental concerns have increased the demand for clean,
46 renewable energy sources. hydrogen is considered as one of the most promising sources and
47 hydrogen fuel cells efficiently convert chemical energy into electrical energy¹. Particularly,
48 low-temperature proton exchange membrane fuel cells (LT-PEMFCs) using perfluorosulfonic
49 acid membranes are appealing alternative power devices for transportation applications
50 because of their low noise, high power density, and long driving distance with a single charge
51 of hydrogen. However, issues such as the demand for high-purity fuel (H₂), cost, lack of
52 membrane and electrode durability, and complicated water management in the electrochemical
53 system hinder the commercialization of proton exchange membrane fuel cells (PEMFCs)^{2,3}.

54 By contrast, high-temperature proton exchange membrane fuel cells (HT-PEMFC) can
55 operate at 140-180 °C and offer several advantages such as significantly enhanced reaction
56 kinetics, high power output, enhanced CO tolerance, and relatively simple water management⁴
57 ⁶. However, the most promising HT-PEMFC based on a phosphoric acid (PA)-doped
58 polybenzimidazole (PBI) membrane showed limited long-term stability up to 180 °C and
59 exhibited unsatisfactory cell performance with a maximum power density of ~0.5 W·cm⁻² at
60 160 °C^{7,8}. As PA is used as an electrolyte, proton conduction is not possible owing to the
61 leakage of PA or the formation of phosphoric anhydride at higher operating temperatures^{9,10}.
62 The suboptimal cell performance and limited operating temperature range make it difficult to
63 adopt such cells for a variety of applications.

64 The purpose of this study is to develop polymer electrolyte membranes that operate at
65 temperature range of 200–250 °C. In this temperature range, extraction of hydrogen from liquid
66 hydrogen carriers (LHCs) such as methanol and N-ethylcarbazole is possible within the fuel
67 cell, which improves fuel cell efficiency. These liquid hydrogen carriers lead to a high

68 volumetric energy density and are compatible with the current fuel storage and transport
69 infrastructure^{11,12}, solving problems of the physical hydrogen storage methods.

70 We consider solid acids promising candidates for use as HT-PEMFC electrolytes working
71 at an integrated high-temperature range (200–300 °C). Many research groups have tried to
72 increase the operating temperature of PEMFCs. The majority of the groups have been
73 developing composite membranes to reduce the evaporation of the electrolyte PA at high
74 temperatures¹³⁻¹⁵. Another group has developed ion-pair-coordinated membrane electrode
75 assemblies focusing on the binder rather than the electrolyte¹⁶⁻¹⁸. Nevertheless, the key
76 challenge in attaining optimal and stable fuel cell performance is stabilizing the proton carrier
77 at temperatures higher than 200 °C. Herein, we report a proton conductor, unique nanofibrous
78 cerium hydrogen phosphate (CeHP, (HCe₂(PO₄)₃(H₂O))) immobilized in a PBI polymer
79 electrolyte, which can overcome the limitations of the state-of-the-art PA-based PEM
80 electrolytes, thereby enabling fuel cell operation over 250 °C. These PEMs can transfer protons
81 through a nanofibrous CeHP network. Notably, the novel membranes have a nanofibrous CeHP
82 network chemically bound to the PBI backbone, resulting in the formation of the hydrogen
83 bond network through which the structural diffusion of protons becomes possible. We
84 evaluated the performance and durability of the novel membrane in the temperature range 150–
85 250 °C. In particular, the significantly improved CO tolerance at high temperatures enables the
86 use of low-purity hydrogen and reformat gases from hydrogen carriers such as methanol and
87 dimethyl ether (DME) through external reforming¹⁹⁻²². Additionally, we have been developing
88 couplings between the H₂ extraction reaction and the electrochemical reaction of a fuel cell by
89 utilizing fuels such as LHCs. As a proof of concept, we evaluated the performance of integrated
90 fuel processor-fuel cells using H₂ from the dehydrogenation of hydrogenated N-ethylcarbazole
91 and methanol reforming.

92 **Self-assembled network PBI membrane fabrication**

93 We synthesized a self-assembled network (SAN) polymer electrolyte membrane using
94 nanofibrous CeHP as a proton conductor through an *in-situ* sol-gel process (the membranes are
95 denoted as SAN-CeHP-PBI). The *in-situ* sol-gel process allows the simple one-pot and low-
96 cost fabrication of large-area membranes²³. CeHP is a unique insoluble acid salt of a tetravalent
97 metal that forms a nanofibrous structure when it is in the phosphate form²⁴⁻²⁶ (**Supplementary**
98 **Discussion 1, Extended Data Fig. 1a and 1b**). When CeHP powder is mixed with
99 concentrated PA, it shows solvation behavior, similar to an ionomer (**Supplementary**
100 **Discussion 1, Extended data Figure 2**). To synthesize SAN-CeHP-PBI, the CeHP (IV)
101 precursor solution was added during the termination process of *p*-PBI polymer synthesis²⁷ (**Fig.**
102 **1a**). The Ce (IV) ions of the added Ce precursor were evenly dispersed in the polymer solution,
103 serving as a nucleus for the formation of a crystal in the polymer. This mixed Ce precursor and
104 *p*-PBI polymer solution were applied to a glass plate, and the electrolyte membrane was
105 prepared by the doctor blade method. Subsequently, water was released during the hydrolysis
106 of the mixed Ce precursor and *p*-PBI electrolyte membrane in the humidified chamber oven,
107 converting polyphosphoric acid to PA and producing nanofibrous CeHP from Ce (IV) ions in
108 the *p*-PBI polymer. Thus, as CeHP and *p*-PBI were synthesized simultaneously, the
109 nanofibrous CeHP structure formed a SAN that stably bound to the *p*-PBI polymer. The results
110 indicate that structural surface diffusion of the proton can be possible within the hydrogen bond
111 network of the SAN-CeHP-PBI polymer.

112 **Working principle of PA-doped SAN-CeHP-PBI**

113 The excess PA-doped SAN-CeHP-PBI composite membranes dominantly follow the PA
114 proton transfer mechanism: a Grotthuss-type hopping mechanism below 180 °C^{10,28} (**Fig. 1b**).
115 Above 200 °C, the SAN polymer electrolyte membrane becomes thinner due to the

116 condensation reaction and leaching of PA and water from the composite membranes doped with
117 excess PA (**Extended Data Fig. 3a, 3b**). The elevated operating temperature results in forming
118 an amorphous $\text{CeH}_x\text{PO}_4(\text{OH})_y$ structure with a small amount of remaining PA and crystalline
119 CeHP. Consequently, the $\text{CeH}_x\text{PO}_4(\text{OH})_y$ generated between the hydrogen bond network of the
120 SAN-CeHP-PBI polymer formed more closely connected SANs, and structural diffusion sites
121 were created above 200 °C (**Fig. 1c**). The dominant proton conduction pathway changed from
122 the PA electrolyte to surface/interfacial conduction in the SAN of the CeHP-PBI polymer, and
123 the concentrated PA-CeHP mixtures held the PA molecules because of better adhesion at the
124 acid/acid salt interface^{11,15} (see **Extended Data Fig.4**). We fabricated membrane electrode
125 assemblies (MEAs) using the SAN-CeHP-PBI membrane, carbon-supported Pt catalysts, and
126 PTFE binder. The single cell was operated at 150–250 °C using H_2/O_2 , and it was found that
127 the performance increased with increasing temperature, with the SAN polymer electrolyte
128 membrane exhibiting a maximum peak power density of $2.4 \text{ W}\cdot\text{cm}^{-2}$ at 250 °C (**Fig. 1d and**
129 **Extended Data Fig. 3c**). This is the best performance obtained among the state-of-the-art fuel
130 cells capable of operating at 200–300 °C, as shown in **Fig. 1e and the Extended Data Table.**
131 **1**^{2,13-16,29-39}.

132 **Property comparison for three type of PA-doped PBI membranes**

133 We compare the properties of three types of PA-doped PBI membranes (*p*-PBI²⁷: the pristine
134 membrane that does not contain Ce, CeHP-PBI, and SAN-CeHP-PBI). The CeHP-PBI
135 composite membrane was prepared by the conventional *ex-situ* method of adding a CeHP
136 nanoparticle powder solution in the *p*-PBI polymer solution^{40,41} (the membranes are denoted
137 as CeHP-PBI). The CeHP nanoparticle powder in PA added during polymerization does not
138 change significantly upon the chemical bonding of polymers even during hydrolysis¹⁰
139 (**Extended Data Fig. 5 and Table. 2**), and CeHP nanoparticle are dispartate in the PA-doped

140 PBI polymer (**Fig. 2a**). When the temperature is below 200 °C, fuel cells with composite
141 membranes doped with excess PA showed higher performance than those prepared with PA-
142 doped pristine p-PBI. Further, protons are conducted by the Grotthuss mechanism through PA
143 (**Fig. 2a and 2b**). However, the excess PA disappears at temperatures above 200 °C, and in
144 the SAN-CeHP-PBI, proton conduction occurs by surface/interfacial conduction and
145 structural diffusion through the SAN of CeHP caused by water molecules and PA bound to
146 CeHP. By contrast, in CeHP-PBI, proton conduction is limited because protons are
147 transported to the dispersed CeHP, which does not form a close network for proton conduction
148 (**Fig. 2c, 2d and Extended Data Fig. 4**). As the operating temperature increases, PA is
149 removed from the polymer, and SEM analysis confirmed the appearance of an amorphous
150 $\text{CeH}_x\text{PO}_4(\text{OH})_y$ and CeHP structure in the CeHP-PBI and SAN-CeHP-PBI membranes.
151 Notably, SAN-CeHP-PBI shows more connected nanofibrous structures than those of CeHP-
152 PBI (**Extended Data Fig. 2 and 5a-d**).

153 We compared the proton conductivities of three types of PA-dope PBI membranes under dry
154 conditions as a function of temperature. The proton conductivity of *p*-PBI is unmeasurable
155 above 200 °C and does not change notably within the temperature range employed in this
156 study. The proton conductivity of CeHP-PBI increased with increasing temperature up to
157 200 °C and then decreased with further temperature increase because of the absence of
158 proton conducting channels^{11,42,43}. Unlike the other two membranes, the proton conductivity
159 of SAN-CeHP-PBI gradually increased with increasing temperature and reached $0.257 \text{ S}\cdot\text{cm}^{-1}$
160 at 280 °C (**Fig. 2e**). In addition, the trend of the high ionic conductivity of SAN-CeHP-
161 PBI can be confirmed with Raman analysis. The Raman spectra of bare SAN-CeHP-PBI
162 displayed a peak at 911 cm^{-1} corresponding to free PA at 30 °C. In the PA-removed de-doped
163 sample, SAN-CeHP-PBI demonstrated a peak at 1632 cm^{-1} at the γ part of the benzimidazole

164 ring of the polymer backbone part. This indicates that in the polymer benzimidazole ring,
165 CeHP is attached to N-H through hydrogen bonding (**Extended Data Fig. 5e-f and Table.**
166 **2**)¹⁰. Further, the combination of polymer-CeHP and CeHP-CeHP network channels in the
167 SAN-CeHP-PBI composite membranes enhances the tensile toughness, which is ~2.5 times
168 (SAN-CeHP-PBI: 3.5 Mpa and de-doped SAN-CeHP-PBI: 125 Mpa) higher than that of
169 pristine *p*-PBI (*p*-PBI: 1.4 Mpa and de-doped *p*-PBI: 50 Mpa) (**Extended Data Fig. 6**).

170 The single-cell performances of three different types of PA-doped membranes were
171 compared under H₂/air conditions without humidification at atmospheric pressure and 150–
172 250 °C , and the results are shown in **Fig. 2f-h**. These membrane electrode assemblies (MEAs)
173 were fabricated by applying commercial BASF electrodes. The fuel cell containing the
174 pristine *p*-PBI membrane could not operate above 200 °C , while the cell containing the CeHP-
175 PBI composite membrane exhibited the maximum power densities 0.93 W·cm⁻² and 0.91
176 W·cm⁻² at 200 °C and 250 °C , respectively. The CeHP-PBI showed the highest performance
177 at 200 °C. By contrast, the performance of the cell with the SAN-CeHP-PBI composite
178 membrane improved with an increase in temperature to 250 °C. The SAN-CeHP-PBI
179 composite membrane exhibited the best performance at 250 °C with the maximum power
180 density of 1.2 W·cm⁻² (1.1 W·cm⁻² at 200 °C).

181 NMR spectroscopic analysis can explain the difference in proton conduction behavior
182 between *p*-PBI, CeHP-PBI, and SAN-CeHP-PBI membranes. The solid-state ³¹P NMR
183 spectra of the three membranes enriched with excess PA exhibit peaks corresponding to
184 H₃PO₄, HPO₄²⁻, and PO₄³⁻ at 0, -14, and -28 ppm, respectively, at 150–280 °C (**Fig. 2i, 2j,**
185 **and 2k**)⁴⁴⁻⁴⁶. The samples show progressive peak broadening with increasing temperature,
186 which is attributed to the exchange of H⁺ ions (or H⁺ hopping) among the three different
187 phosphate phases. The three resonances would merge into a single resonance when the

188 hopping rate increases over the NMR observation time scale, which is of the order of
189 milliseconds. For *p*-PBI and CeHP-PBI, peak broadening was observed until 200 °C, beyond
190 which, interestingly, the peaks sharpened, indicating interference in proton conduction above
191 200 °C (**Fig. 2i and 2j**). On the other hand, peak broadening continued until 280 °C only in
192 SAN-CeHP-PBI as H⁺ ion hopping continued to rise at high temperatures (**Fig. 2k**). Moreover,
193 we analyzed de-doped membranes by solid-state ³¹P NMR analysis, where excessive PA was
194 discarded from the membrane to leave only PA units that are tied with the electrostatic
195 bonding to the PBI polymer chains. The NMR analysis results indicate the proton transfer
196 phenomenon for SAN-CeHP-PBI, from which PA was removed under high-temperature
197 conditions. Typically, the removal of excess phosphoric acid results in the formation of
198 pyrophosphoric acid, which interferes with proton conduction. Unlike in *p*-PBI and CeHP-
199 PBI, pyrophosphoric acid was not formed until 270 °C, and only the Ce(PO₄)₂ peak appeared
200 in SAN-CeHP-PBI. This may be due to the mobility of the polymer matrix at high
201 temperatures, which was beneficial to the transport of the H⁺ ions in the structure (**Extended**
202 **Data Fig. 7 Supplementary Discussion 2**). The de-doped SAN-CeHP-PBI composite
203 membrane was re-doped, and its single cell performance was tested to see the reversibility of
204 PA doping. Although re-doped SAN-CeHP-PBI exhibited a lower performance due to the
205 change in PA acid doping level (PA-doped 40 PA/PBI RU to re-doped 32 PA/PBI RU), the
206 performance was stable for 5,000 min. The strong bond between the synthesized SAN-CeHP
207 channel and PBI is not dissociated by PA leakage (**Extended Data Fig. 8**).

208 **Effect of Ce content for SAN-CeHP-PBI membranes**

209 We synthesized membranes with 0-90 wt% Ce content compared to the polymer monomer to
210 optimize SAN channel formation. The CeHP structures and the degree of crystallinity depend
211 on the concentration of solutions containing a Ce(IV) salt and the [PO₄/Ce(IV) ratio]^{25,26}.

212 **Figure 3a** shows SEM images of the networking morphology of SAN-CeHP-PBI membranes
213 according to different contents of Ce. The larger the Ce content, the larger the crystal size due
214 to the agglomeration of Ce molecules. However, if the amount of Ce is 70 wt% or more for the
215 same PA solution, the proportion of PO_4^{3-} that can react with the Ce(IV) precursor becomes
216 relatively small. Therefore, as the amount of Ce exceeds 70 wt%, crystalline growth by
217 nucleation becomes limited, and a non-fibrous morphology and smaller and widely distributed
218 crystalline size are observed. At 35 wt% Ce content, a semi-crystalline polymer with a dense
219 fibrous self-assembled network structure was formed by the growth of spherulites from the
220 crystalline nuclei derived from the Ce precursor (**Fig. 3a**). The acid doping level of 35 wt%
221 SAN-CeHP-PBI is 40 mol H_3PO_4 /PBI repeat unit, which is 1.6 times higher than those of
222 conventional PA-doped *p*-PBI and CeHP-PBI (27.7 and 26 PA/PBI RU). Additionally, NMR
223 quantitation of ^{31}P signals of the H_3PO_4 , HPO_4^{2-} , and PO_4^{3-} phases normalized by the weight of
224 all the samples was performed, and the highest NMR quantitation was obtained for the
225 membrane with 35 wt% Ce content (**Fig. 3b**). The hopping effect of protons was the highest in
226 15 wt% SAN-CeHP-PBI (**Fig. 3c**), but the mechanical strength of 35 wt% SAN-CeHP-PBI
227 was superior to that of other composite membranes owing to the close interactions
228 corresponding to crystalline CeHP (**Fig. 3d and 3e**).

229 **Fuel cell performances and durability**

230 The best H_2 /air fuel cell performance was achieved with 35 wt% SAN-CeHP-PBI at 250 °C,
231 with a maximum power density of $1.16 \text{ W}\cdot\text{cm}^{-2}$ (**Extended Data Fig. 9a-c**). This is attributed
232 to the proton transfer channels formed by the dense fibrous morphology of CeHP. We prepared
233 with MEAs using optimized 35 wt% SAN-CeHP-PBI membranes, carbon-supported Pt
234 catalysts, and PTFE binder. CO tolerance tests were conducted by supplying H_2 /air or a mixture
235 of 10% CO and H_2 /air to the anode at different temperatures, and the fuel cell voltage was

236 recorded at a constant current density of $0.2 \text{ A}\cdot\text{cm}^{-2}$ for 2,250 min. As shown in **Fig. 3f**, the
237 voltage slightly decreased from 0.78 at 250 °C to 0.71 V at 160 °C. This improved CO tolerance
238 of the 35 wt% SAN-CeHP-PBI membranes allows the direct use of the reformation of liquid
239 fuels. The long-term durability test of 35 wt% SAN-CeHP-PBI MEAs was performed at 0.2
240 $\text{A}\cdot\text{cm}^{-2}$ and 250 °C under H_2 /air conditions, showing a highly stable performance for 7,000 min
241 at 250 °C (**Fig. 3g**). Electrochemical impedance spectroscopy (EIS) was performed at 0.85 V
242 and 0.6 V, respectively, to compare the performances of 35 wt% SAN-CeHP-PBI MEAs before
243 and after the durability test. The ohmic resistances ($0.013 \text{ }\Omega\cdot\text{cm}^2$ to $0.018 \text{ }\Omega\cdot\text{cm}^2$) at 0.85 V and
244 0.6 V are similar before and after the durability test, whereas the charge transfer resistance is
245 increased slightly after the durability test⁴⁷ (**Extended Data Fig. 10**). This indicates that MEA
246 degradation is caused by the electrode degradation (especially, Pt/C and PTFE binder) rather
247 than the PEM at a high operating temperature of 250 °C over a long period⁴⁸. Therefore,
248 catalysts and binders that are stable in the operating temperature ranges must be developed for
249 long-term HT-PEMFCs operating at 200–300 °C.

250 **Performance of HT-PEMFC integrated with H_2 extraction system**

251 Integration of the as-developed fuel cell with an external H_2 extraction system using LHCs
252 demonstrated the viability of an ideal direct LHC fuel cell concept (see **Supplementary**
253 **Discussion 3**). However, in a single cell, it is difficult to experimentally demonstrate the effects
254 of heat and mass transfer integration, as heat loss is larger than exchanged heat. Therefore,
255 external reforming was demonstrated by physically attaching the reforming unit to the single
256 cell while maintaining the same temperature for the fuel cell and the reformer to simulate a
257 heat-integrated configuration (**Extended Data Fig. 11c and 11d**). We compared the fuel cell
258 performances of pure H_2 and as-produced H_2 from the reformer by varying the flow rate of a
259 small-scale single cell. First, an N-ethylcarbazole (NEC) dehydrogenation external reformer

260 was built that was operated in conjunction with the single cell. No difference in performance
261 (power density: $0.5 \text{ W}\cdot\text{cm}^{-2}$) was observed, as expected. The result is encouraging with regards
262 to the feasibility of heat management based on integration, and thus, the viability of a direct-
263 LHC fuel cell (**Fig. 4a**). Second, methanol was used to benchmark the performance of the fuel
264 cell. The composition of the fuel provided to the anode was varied: 100% pure H_2 , 50% pure
265 H_2 , and 50% off-gas, and 100% off-gas from the external reformer. The performances of the
266 fuel cells using three different fuel compositions were almost the same (power density: 0.82
267 $\text{W}\cdot\text{cm}^{-2}$) (**Fig. 4b**), which shows the viability of external methanol reforms coupled with the
268 developed fuel cell. Moreover, at $250 \text{ }^\circ\text{C}$, high conversion of methanol ($>90\%$) was achieved.
269 Finally, long-term durability experiments were conducted to determine whether the external
270 reforming of methanol is a viable option to provide H_2 -rich fuel containing CO. The results
271 showed that the external reforming methanol fuel cell is stable under 3% CO and $0.5 \text{ A}\cdot\text{cm}^{-2}$
272 for 1200 min at $250 \text{ }^\circ\text{C}$ (**Fig. 4c**). The SAN-CeHP-PBI-based PEMFC combined with the
273 reformed LHC fuel demonstrated exceptional CO tolerance and long-term durability at $250 \text{ }^\circ\text{C}$.
274 Moreover, it highlighted that this technology is promising and has the potential for commercial
275 application. We suggest a conceptual direct LHC system, extending the range of heavy-duty
276 trucks powered with integrated HT-PEMFC stacks fueled by LHCs, in contrast with fueling by
277 H_2 gas tanks. Based on the preliminary integration work presented in this paper, the combined
278 fuel processor and fuel cell is expected to be a promising device for solving energy density and
279 infrastructural problems related to compressed H_2 ⁴⁹ (**Fig. 4d**).

280 **Conclusions**

281 In summary, we developed HT-PEMFCs based on a new type of proton carrier, SAN-CeHP-
282 PBI PEMs, in which proton conduction occurs through a self-assembled network of CeHP. At
283 operating temperatures above $180 \text{ }^\circ\text{C}$, the dominant proton conduction pathway changed from

284 the PA electrolyte to surface/interfacial conduction in the SAN CeHP-PBI polymer, thereby
285 overcoming the limitations of PA-based PEM electrolytes and enabling operation at 250 °C.
286 The SAN-CeHP-PBI membrane exhibited the best performance among all the excellent fuel
287 cells operating at 250 °C reported so far, as well as excellent CO tolerance, thus showing great
288 promise for high-performance integration energy applications at high temperatures (up to
289 280 °C). The SAN-CeHP-PBI membranes afford an integrated fuel cell–internal reforming
290 system that can be applied to mobility solutions. This shows the feasibility of heat integration
291 and the viability of a direct-LHC fuel cell and its potential for commercial application. Other
292 challenges are developing stable catalysts and binders to withstand long-term operation and
293 exposure to temperatures above 250 °C.

294

295 **References**

- 296 1 Lemmon, J. P. Energy: Reimagine fuel cells. *Nature News* **525**, 447 (2015).
- 297 2 Park, C. H. *et al.* Nanocrack-regulated self-humidifying membranes. *Nature* **532**, 480-
298 483 (2016).
- 299 3 Steele, B. C. & Heinzel, A. in *Materials for sustainable energy: a collection of peer-*
300 *reviewed Research and review articles from nature publishing group* 224-231
301 (World Scientific, 2011).
- 302 4 Alberti, G., Casciola, M., Massinelli, L. & Bauer, B. Polymeric proton conducting
303 membranes for medium temperature fuel cells (110–160 C). *Journal of Membrane*
304 *Science* **185**, 73-81 (2001).
- 305 5 Li, Q., He, R., Jensen, J. O. & Bjerrum, N. J. Approaches and recent development of
306 polymer electrolyte membranes for fuel cells operating above 100 C. *Chemistry of*
307 *materials* **15**, 4896-4915 (2003).

- 308 6 Zhang, J. *et al.* High temperature PEM fuel cells. *Journal of power Sources* **160**, 872-
309 891 (2006).
- 310 7 Moçotéguy, P. *et al.* Long-Term Testing in Dynamic Mode of HT-PEMFC H3PO4/PBI
311 Celtec-P Based Membrane Electrode Assemblies for Micro-CHP Applications. *Fuel*
312 *Cells* **10**, 299-311 (2010).
- 313 8 Yu, S., Xiao, L. & Benicewicz, B. Durability studies of PBI-based high temperature
314 PEMFCs. *Fuel Cells* **8**, 165-174 (2008).
- 315 9 Schuster, M., Rager, T., Noda, A., Kreuer, K. & Maier, J. About the choice of the
316 protogenic group in PEM separator materials for intermediate temperature, low
317 humidity operation: a critical comparison of sulfonic acid, phosphonic acid and
318 imidazole functionalized model compounds. *Fuel Cells* **5**, 355-365 (2005).
- 319 10 Melchior, J.-P., Majer, G. & Kreuer, K.-D. Why do proton conducting
320 polybenzimidazole phosphoric acid membranes perform well in high-temperature PEM
321 fuel cells? *Physical Chemistry Chemical Physics* **19**, 601-612 (2017).
- 322 11 Zhang, J., Xiang, Y., Lu, S. & Jiang, S. P. High temperature polymer electrolyte
323 membrane fuel cells for integrated fuel cell–methanol reformer power systems: a
324 critical review. *Advanced Sustainable Systems* **2**, 1700184 (2018).
- 325 12 Papavasiliou, J., Avgouropoulos, G. & Ioannides, T. CuMnOx catalysts for internal
326 reforming methanol fuel cells: Application aspects. *International journal of hydrogen*
327 *energy* **37**, 16739-16747 (2012).
- 328 13 Li, X. *et al.* Construction of high-performance, high-temperature proton exchange
329 membranes through incorporating SiO2 nanoparticles into novel cross-linked
330 polybenzimidazole networks. *ACS applied materials & interfaces* **11**, 30735-30746
331 (2019).

- 332 14 Lobato, J., Canizares, P., Rodrigo, M. A., Úbeda, D. & Pinar, F. J. Enhancement of the
333 fuel cell performance of a high temperature proton exchange membrane fuel cell
334 running with titanium composite polybenzimidazole-based membranes. *Journal of*
335 *Power Sources* **196**, 8265-8271 (2011).
- 336 15 Zhang, J. *et al.* In situ formed phosphoric acid/phosphosilicate nanoclusters in the
337 exceptional enhancement of durability of polybenzimidazole membrane fuel cells at
338 elevated high temperatures. *Journal of the Electrochemical Society* **164**, F1615 (2017).
- 339 16 Lee, K.-S. *et al.* Intermediate temperature fuel cells via an ion-pair coordinated polymer
340 electrolyte. *Energy & Environmental Science* **11**, 979-987 (2018).
- 341 17 Lee, K.-S., Spendelow, J. S., Choe, Y.-K., Fujimoto, C. & Kim, Y. S. An operationally
342 flexible fuel cell based on quaternary ammonium-biphosphate ion pairs. *Nature energy*
343 **1**, 1-7 (2016).
- 344 18 Atanasov, V. *et al.* Synergistically integrated phosphonated poly (pentafluorostyrene)
345 for fuel cells. *Nature Materials* **20**, 370-377 (2021).
- 346 19 Orfanidi, A., Daletou, M. K. & Neophytides, S. G. Mitigation strategy towards
347 stabilizing the Electrochemical Interface under high CO and H₂O containing reformat
348 gas feed. *Electrochimica Acta* **233**, 218-228 (2017).
- 349 20 Geormezi, M. *et al.* The structure and stability of the anodic electrochemical interface
350 in a high temperature polymer electrolyte membrane fuel cell under reformat feed.
351 *Journal of Power Sources* **285**, 499-509 (2015).
- 352 21 Zhang, C., Zhou, W., Ehteshami, M. M., Wang, Y. & Chan, S. H. Determination of the
353 optimal operating temperature range for high temperature PEM fuel cell considering its
354 performance, CO tolerance and degradation. *Energy conversion and management* **105**,
355 433-441 (2015).

- 356 22 Li, Q., He, R., Gao, J.-A., Jensen, J. O. & Bjerrum, N. J. The CO poisoning effect in
357 PEMFCs operational at temperatures up to 200 C. *Journal of the Electrochemical*
358 *Society* **150**, A1599 (2003).
- 359 23 Xiao, L. *et al.* High-temperature polybenzimidazole fuel cell membranes via a sol–gel
360 process. *Chemistry of Materials* **17**, 5328-5333 (2005).
- 361 24 Alberti, G., Constantino, U., Di Gregorio, F., Galli, P. & Torracca, E. Crystalline
362 insoluble salts of polybasic metals-III: Preparation and ion exchange properties of
363 cerium (IV) phosphate of various crystallinities. *Journal of Inorganic and Nuclear*
364 *Chemistry* **30**, 295-304 (1968).
- 365 25 Albert, G. & Costantino, U. Crystalline insoluble acid salts of tetravalent metals: X.
366 Fibrous thorium phosphite, a new inorganic ion-exchange material suitable for making
367 (support-free) inorganic sheets. *Journal of Chromatography A* **50**, 482-486 (1970).
- 368 26 Shakshooki, S., El-Akari, F., El-Fituri, S. & El-Fituri, S. in *Advanced Materials*
369 *Research*. 3-8 (Trans Tech Publ).
- 370 27 Lee, J. W. *et al.* Synthesis and characterization of acid-doped polybenzimidazole
371 membranes by sol–gel and post-membrane casting method. *Journal of Membrane*
372 *Science* **357**, 130-133 (2010).
- 373 28 Ma, Y.-L., Wainright, J., Litt, M. & Savinell, R. Conductivity of PBI membranes for
374 high-temperature polymer electrolyte fuel cells. *Journal of the Electrochemical Society*
375 **151**, A8 (2003).
- 376 29 Li, J. *et al.* High-Temperature Proton-Exchange-Membrane Fuel Cells Using an Ether-
377 Containing Polybenzimidazole Membrane as Electrolyte. *ChemSusChem* **5**, 896-900
378 (2012).
- 379 30 Lobato, J., Cañizares, P., Rodrigo, M. A., Úbeda, D. & Pinar, F. J. Promising TiOSO₄

- 380 Composite Polybenzimidazole-Based Membranes for High Temperature PEMFCs.
381 *ChemSusChem* **4**, 1489-1497 (2011).
- 382 31 Li, X. *et al.* Highly conductive and mechanically stable imidazole-rich cross-linked
383 networks for high-temperature proton exchange membrane fuel cells. *Chemistry of*
384 *Materials* **32**, 1182-1191 (2020).
- 385 32 Singh, B. *et al.* High temperature polymer electrolyte membrane fuel cells with
386 Polybenzimidazole-Ce_{0.9}Gd_{0.1}P₂O₇ and polybenzimidazole-Ce_{0.9}Gd_{0.1}P₂O₇-
387 graphite oxide composite electrolytes. *Journal of Power Sources* **401**, 149-157 (2018).
- 388 33 Sun, X. *et al.* Proton conductivity of CeP₂O₇ for intermediate temperature fuel cells.
389 *Solid State Ionics* **179**, 1138-1141 (2008).
- 390 34 Chen, X. *et al.* A proton conductor electrolyte based on molten CsH₅(PO₄)₂ for
391 intermediate-temperature fuel cells. *RSC advances* **8**, 5225-5232 (2018).
- 392 35 Jensen, A. H., Li, Q., Christensen, E. & Bjerrum, N. J. Intermediate temperature fuel
393 cell using CsH₂PO₄/ZrO₂-based composite electrolytes. *Journal of the*
394 *Electrochemical Society* **161**, F72 (2013).
- 395 36 Nagao, M. *et al.* A proton-conducting In³⁺-doped SnP₂O₇ electrolyte for intermediate-
396 temperature fuel cells. *Electrochemical and Solid State Letters* **9**, A105 (2006).
- 397 37 Uda, T. & Haile, S. M. Thin-membrane solid-acid fuel cell. *Electrochemical and Solid*
398 *State Letters* **8**, A245 (2005).
- 399 38 Duan, C. *et al.* Readily processed protonic ceramic fuel cells with high performance at
400 low temperatures. *Science* **349**, 1321-1326 (2015).
- 401 39 Hibino, T. *et al.* A low-operating-temperature solid oxide fuel cell in hydrocarbon-air
402 mixtures. *Science* **288**, 2031-2033 (2000).
- 403 40 Seo, K., Nam, K.-H. & Han, H. proton transport in Aluminum-Substituted Mesoporous

404 Silica channel-embedded High-temperature Anhydrous proton-exchange Membrane
405 fuel cells. *Scientific reports* **10**, 1-9 (2020).

406 41 Li, Y. *et al.* Recent advances in the fabrication of advanced composite membranes.
407 *Journal of Materials Chemistry A* **1**, 10058-10077 (2013).

408 42 Jensen, J. O., Li, Q., He, R., Pan, C. & Bjerrum, N. 100–200° C polymer fuel cells for
409 use with NaAlH₄. *Journal of alloys and compounds* **404**, 653-656 (2005).

410 43 Mustarelli, P., Quartarone, E., Grandi, S., Carollo, A. & Magistris, A.
411 Polybenzimidazole-Based Membranes as a Real Alternative to Nafion for Fuel Cells
412 Operating at Low Temperature. *Advanced Materials* **20**, 1339-1343 (2008).

413 44 Bhavsar, R. S., Kumbharkar, S. C., Rewar, A. S. & Kharul, U. K. Polybenzimidazole
414 based film forming polymeric ionic liquids: synthesis and effects of cation–anion
415 variation on their physical properties. *Polymer Chemistry* **5**, 4083-4096 (2014).

416 45 Zhao, L. *et al.* Imidazole-doped cellulose as membrane for fuel cells: structural and
417 dynamic insights from solid-state NMR. *The Journal of Physical Chemistry C* **120**,
418 19574-19585 (2016).

419 46 Goward, G. R., Schuster, M. F., Sebastiani, D., Schnell, I. & Spiess, H. W. High-
420 resolution solid-state NMR studies of imidazole-based proton conductors: Structure
421 motifs and chemical exchange from ¹H NMR. *The Journal of Physical Chemistry B*
422 **106**, 9322-9334 (2002).

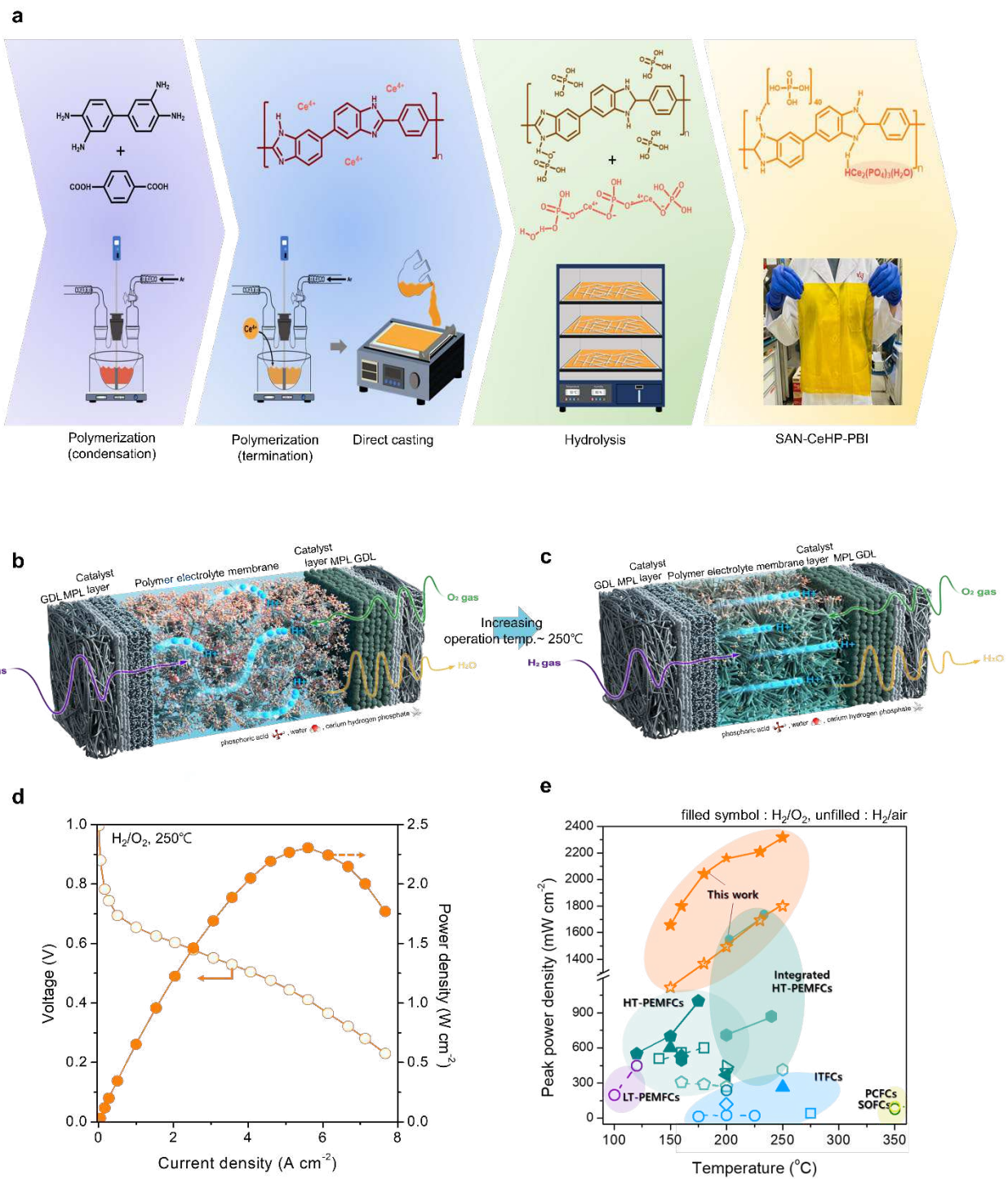
423 47 Zhang, J. *et al.* PEM fuel cells operated at 0% relative humidity in the temperature
424 range of 23–120 C. *Electrochimica Acta* **52**, 5095-5101 (2007).

425 48 Mamlouk, M. & Scott, K. The effect of electrode parameters on performance of a
426 phosphoric acid-doped PBI membrane fuel cell. *International journal of hydrogen*
427 *energy* **35**, 784-793 (2010).

428 49 Staffell, I. *et al.* The role of hydrogen and fuel cells in the global energy system. *Energy*
429 *& Environmental Science* **12**, 463-491 (2019).

430

431



432

433 **Figure 1 | Self-assembled network polymer electrolyte membrane**

434 **a**, The formation of self-assembled network polymer electrolyte membrane; Chemical structure

435 of SAN-CeHP-PBI membrane and schematic diagram of the *in-situ* sol-gel process. (30 cm ×

436 30 cm, 110 μm). **b,c**, Scheme for the operating principle of PA doped SAN-CeHP-PBI
437 composite membranes; formation of cerium hydrogen phosphate proton pathway structures and
438 its role in the stabilization of proton conduction (c) at below 180°C and (d) at elevated high
439 temperature of over 200 °C. **d**, H₂/O₂ fuel cell performance, *i*-V curve with Pt/C (1.5 mg_{Pt}·cm⁻²)
440 and the PA doped SAN-CeHP-PBI composite membrane (*t* = 110 μm) at 250 °C under 3 bar
441 without humidification. **e**, Performance comparison of different types of fuel cells; filled
442 symbol: H₂/O₂; unfilled: H₂/Air.

443

444

445

446

447

448

449

450

451

452

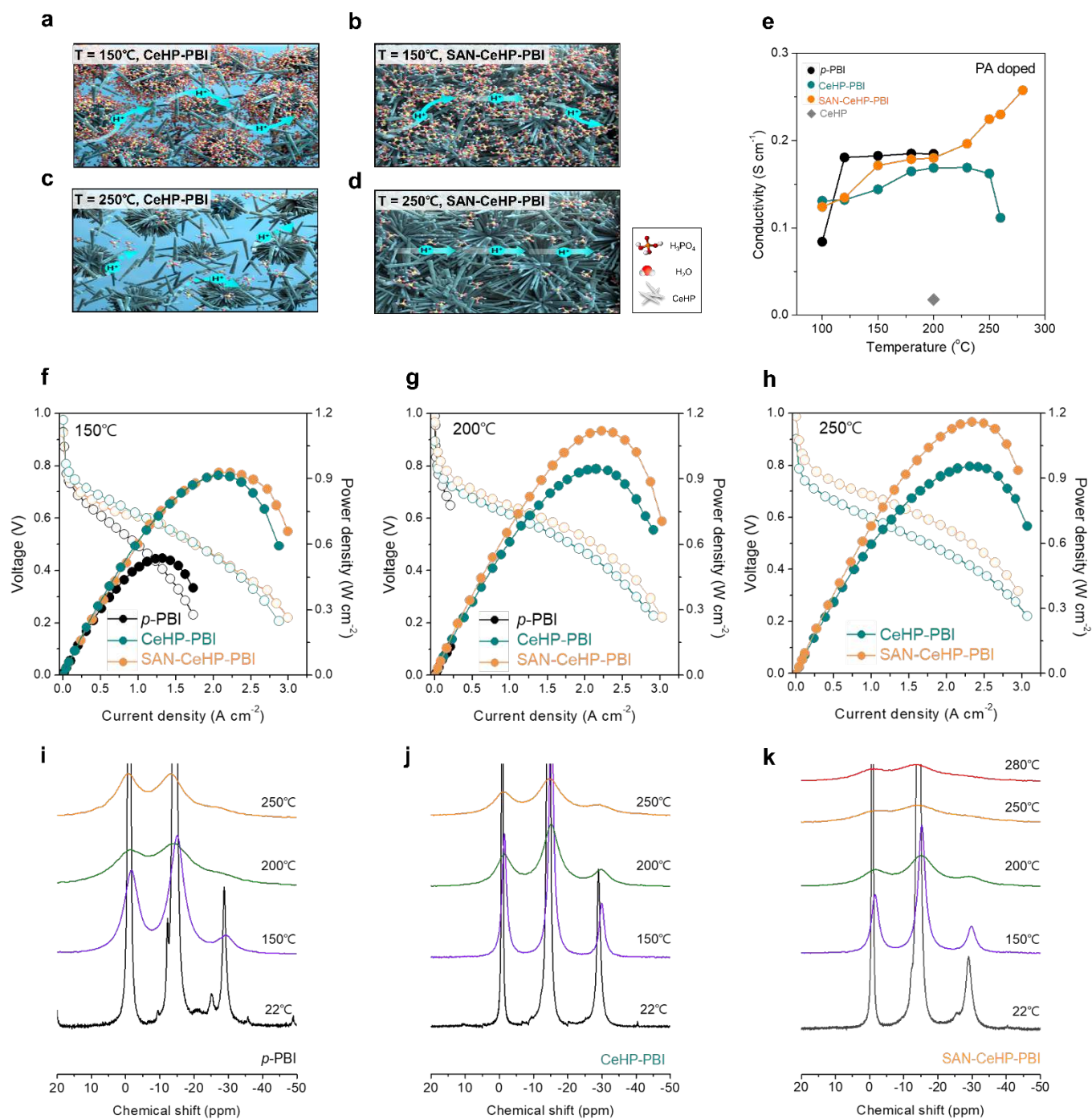
453

454

455

456

457



458

459 **Figure 2 | Role of self-assembled network**

460 **a-d**, Scheme of proton conducting path in composite membrane: CeHP-PBI composite

461 membrane at (a) 150°C and (b) 250°C in comparison with SAN-CeHP-PBI composite

462 membrane at (c) 150°C and (d) 250°C; formation of cerium hydrogen phosphate nanofibrous
463 structure during polymerization to form the attached and stabilized self-assembled network
464 channels anchored in PBI. **e**, Through-plane proton conductivity of SAN-CeHP-PBI composite
465 membranes in comparison with *p*-PBI membrane, CeHP-PBI composite membrane, and
466 Cerium hydrogen phosphate sheet under dry conditions as a function of temperature. **f-h**,
467 H₂/Air fuel cell performance, with Pt/C (2.0 mg_{Pt}·cm⁻², BASF commercial electrode) and the
468 (f) *p*-PBI membrane (*t* = 110μm), (g) CeHP-PBI composite membrane (*t* = 110μm) and (h)
469 SAN-CeHP-PBI composite membrane (*t* = 110μm) with no backpressure at 150-250 °C . **i-k**,
470 ³¹P solid-state MAS NMR spectra of (i) *p*-PBI membrane, (j) CeHP-PBI composite membrane,
471 and (k) SAN-CeHP-PBI composite membrane shown for all three samples as T rises.

472

473

474

475

476

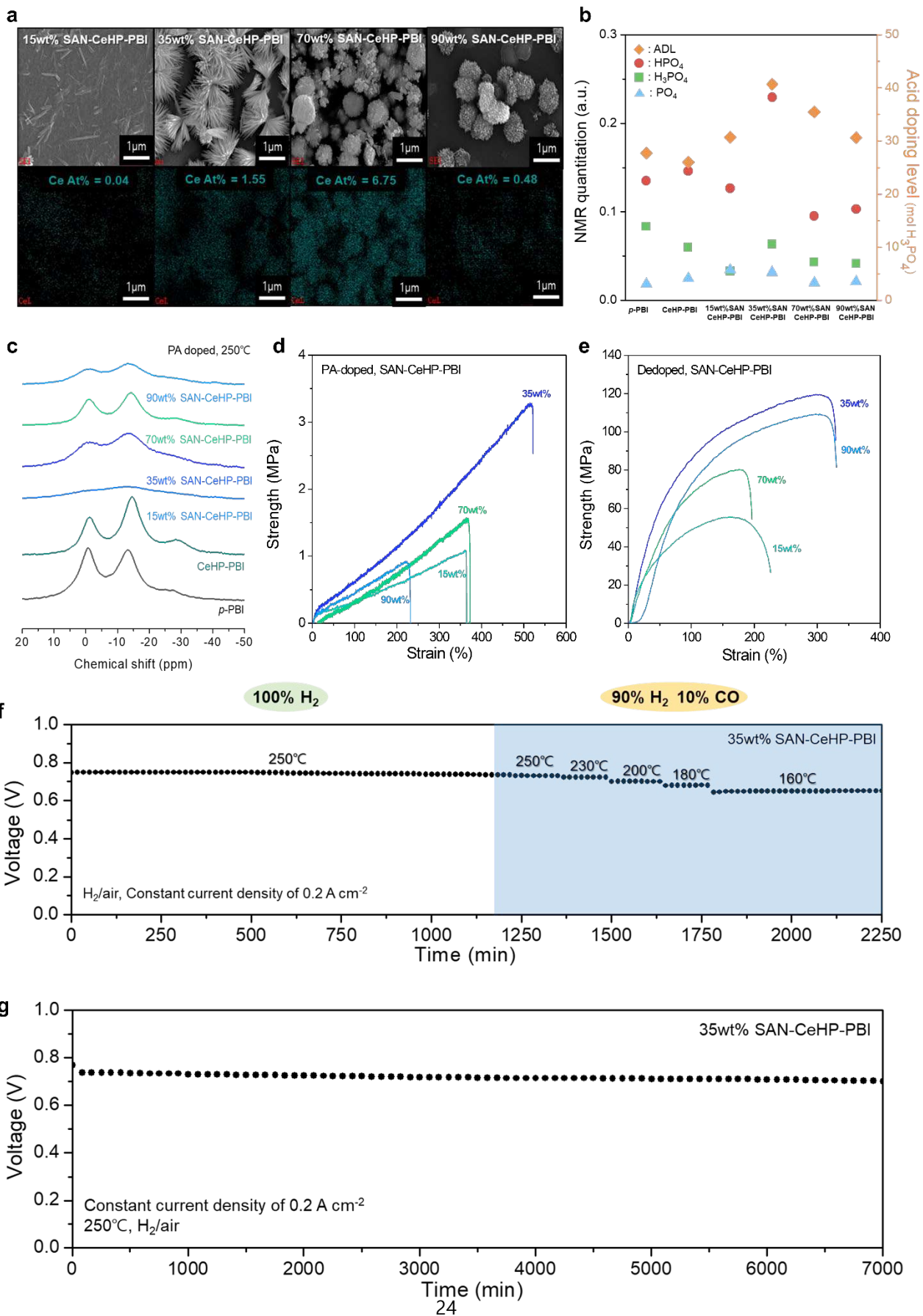
477

478

479

480

481



483 **Figure 3 | Optimization of cerium content for high performance and durability**
484 **a**, Scanning electron microscope images and EDX mapping images of Ce element; the various
485 De-doped SAN-CeHP-PBI composite membranes with 15, 35, 70, and 90 wt% Cerium
486 precursor. **b**, Acid doping level (mol H₃PO₄/unit of PBI) and NMR quantitation of ³¹P signals
487 for H₃PO₄, HPO₄, and PO₄ phases normalized by the weight of all the samples: ADL, ◆; H₃PO₄,
488 ■; HPO₄, ●; PO₄, ▲. **c**, ³¹P solid-state MAS NMR spectra of the various PA-doped SAN-CeHP-
489 PBI composite membranes with 15, 35, 70 and 90 wt% Cerium precursor at 250°C. **d-e**, Tensile
490 property comparison of the membrane with various cerium contents (d) PA-doped and (e) De-
491 doped SAN-CeHP-PBI composite membranes with 15, 35, 70, and 90 wt% Cerium precursor
492 **f**, Fuel cell performance under the flow of H₂ containing 10% CO versus air at different
493 temperatures. The Pt/C electrodes (1.5 mg_{Pt}·cm⁻²) and 35wt% SAN-CeHP-PBI composite
494 membrane (*t* = 110 μm) were used. **g**, Long-term stability of the fuel cell with 35wt% SAN-
495 CeHP-PBI composite membrane (*t* = 110 μm) at a constant current density of 0.2 A·cm⁻² and
496 250 °C under H₂/air flow without humidification. The fuel cell was prepared with Pt/C
497 electrode (1.5 mg_{Pt}·cm⁻²).

498

499

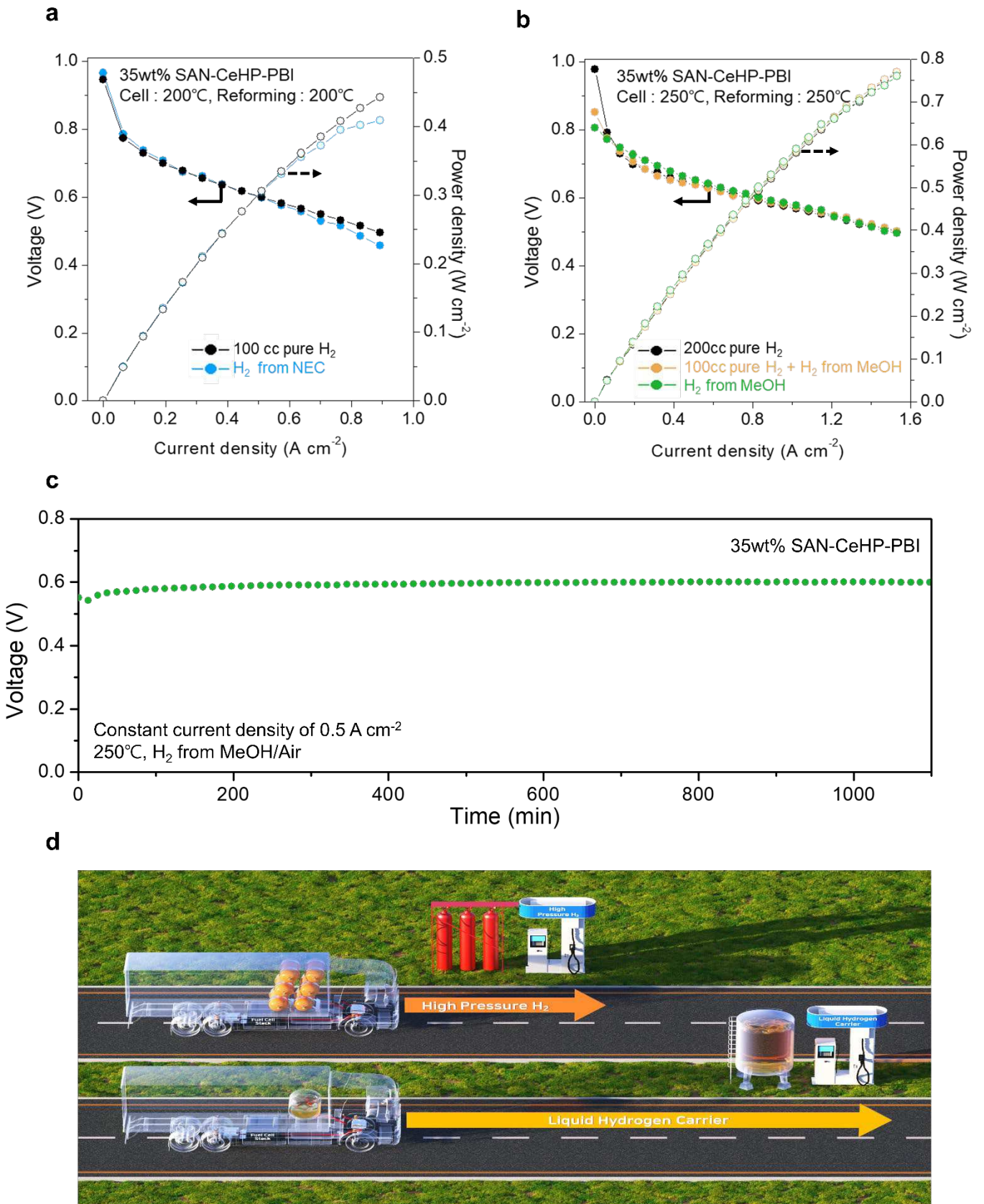
500

501

502

503

504



506 **Figure 4 | Performance of HT-PEMFC integrated with H₂ extraction unit**

507 **a**, *i*-V curve of the single cell with Pt/C electrodes ($1.5 \text{ mg}_{\text{Pt}} \cdot \text{cm}^{-2}$) and PA-doped 35 wt% SAN-
508 CeHP-PBI composite membrane using fuel with 100 sccm pure H₂ and 100 sccm H₂ from the
509 dehydrogenation of hydrogenated N-ethylcarbazole. Both the fuel cell and the dehydrogenation
510 unit attached directly to the fuel cell were maintained at 200 °C. **b**, *i*-V curve of the single-cell
511 with Pt/C electrodes ($1.5 \text{ mg}_{\text{Pt}} \cdot \text{cm}^{-2}$) and PA-doped 35 wt% SAN-CeHP-PBI composite
512 membrane using 200 sccm pure H₂, 100 sccm pure H₂ + 100 sccm H₂-rich gas from methanol
513 reforming, and 200 sccm H₂-rich gas from methanol reforming. Both the fuel cell and the
514 reforming unit attached directly to the fuel cell were maintained at 250 °C, and the CO content
515 in the H₂-rich gas before entering the fuel cell was 1–3 vol%. **c**, Long-term stability of the fuel
516 cell with PA-doped 35 wt% SAN-CeHP-PBI composite membrane ($t = 110 \text{ } \mu\text{m}$) using Pt/C
517 electrodes ($1.5 \text{ mg}_{\text{Pt}} \cdot \text{cm}^{-2}$). The fuel cells were tested at a constant current density of $0.5 \text{ A} \cdot \text{cm}^{-2}$
518 and 250 °C using H₂-rich gas and air under anhydrous conditions, and the CO content in the
519 H₂-rich gas before entering the fuel cell was 1–3 vol%. **d**, Schematic diagram of integrated
520 system application; Extended long-range heavy-duty trucks powered with HT-PEMFC stacks
521 to which H₂ is supplied from H₂ gas tanks or by LHCs.

522 **Methods**

523 **Materials.** 3,3'-Diaminobenzidine (DAB, Alfa Aesar) and terephthalic acid (TPA, Sigma-
524 Aldrich) were dried at 60 °C for one day under a vacuum. Cerium (IV) sulphate tetrahydrate,
525 PPA (115% phosphoric acid equivalent, Sigma-Aldrich), PA solution (85 wt% in H₂O, Sigma-
526 Aldrich), and sulfuric acid (99.9%, Sigma-Aldrich) were purchased and used as received. Pt/C
527 catalyst (46.2 wt%, TANAKA, Japan), gas diffusion electrodes (GDEs, 38BC, SGL), and
528 polytetrafluoroethylene (60 wt% dispersion in H₂O, Sigma-Aldrich) were used to fabricate the
529 anodes. BASF commercial electrodes: Pt/C (Pt loading: 1.0 mg_{Pt}·cm⁻²) were used as anodes,
530 and Pt-alloy/C (Pt loading: 1.0 mg_{Pt}·cm⁻²) were used as cathodes.

531
532 **Synthesis of cerium (IV) hydrogen phosphates (HCe₂(PO₄)₃(H₂O)).** Cerium(IV) hydrogen
533 phosphate was synthesized as described in a previous paper²⁶. Cerium(IV) sulphate tetrahydrate
534 (2.02 g) was dissolved in 100 mL of 0.5 M H₂SO₄. Then, 100 mL of 6 M H₃PO₄ was added
535 dropwise to the solution under stirring at 80 °C. After complete addition, the mixture was allowed
536 to digest at this temperature for 4 h. Subsequently, 1 L of distilled water (~60 °C) was added with
537 stirring for 1 h. The yellow product was washed several times with distilled water, filtered, and
538 dried at 50 °C for 24 h in a convection oven.

539
540 **Synthesis of SAN-CeHP-PBI polymer and membrane fabrication.** An *in-situ* sol-gel process
541 was employed to fabricate the SAN-CeHP-PBI polymer membranes²⁷. DAB (3.0 g, 0.014 mol),
542 TPA (2.3 g, 0.014 mol), and PPA (125 g) were mixed in a round-bottom flask and stirred using
543 a mechanical overhead stirrer for 15 h at 150 °C under argon atmosphere. The reaction
544 temperature was then increased to 220 °C, and the mixture was maintained at this temperature

545 for 1 h. During polymerization, the reaction mixture became viscous and turned dark brown.
546 Then, 25 mL of PA solution was poured into the reaction mixture to terminate the reaction.
547 Finally, cerium(IV) sulphate tetrahydrate (by mass ratio to the polymer monomer) was added,
548 and the mixture was stirred for 2 h. Upon completion of the reaction, the polymerization solution
549 was applied to a glass plate, and the electrolyte membrane with a uniform thickness was prepared
550 by the doctor blade method. The electrolyte membrane was then placed in a temperature and
551 humidity-controlled chamber (at 50 °C and 50% humidity) for one day to obtain PA-doped
552 SAN-CeHP-PBI for MEA fabrication.

553

554 **Synthesis of CeHP-PBI and pristine *p*-PBI polymer and membrane fabrication.** This
555 synthesis is almost the same as the SAN-CeHP-PBI membrane fabrication described above.
556 However, CeHP was added instead of the Ce precursor during the termination process. In the
557 pristine *p*-PBI, the reaction was terminated by adding PA at the end of the reaction without adding
558 any other additive.

559

560 **Proton conductivity measurement.** The ionic conductivity of the membrane samples with
561 dimensions of 1 cm × 4 cm was measured by four-point-probe-based alternating current
562 impedance spectroscopy in the frequency range of 50 kHz to 1 MHz using a Bio-Logic SAS
563 instrument with EC-lab software (Knoxville, TN, USA). The temperature was controlled by a
564 fuel cell station (CNL, Seoul, Korea) under nitrogen flow. The relative humidity of the
565 conductivity cell was maintained at 0%. The through-plane conductivity of all the membrane
566 samples was measured, and the proton conductivity (σ) was calculated from the following
567 equation:

568

$$\sigma = \frac{L}{RS}$$

569

570

571

572

573

574

575

576

577

Structure and morphology characterization. Field-emission scanning electron microscopy and EDX mapping (Teneo VS, FEI, USA) were performed to analyze the surface and cross-sections of the PA-doped and de-doped membrane samples and CeHP sheets. X-ray diffractometer (D8 ADVANCE, LynxEye) patterns of the samples were obtained using monochromic CuK α radiation obtained at 40 kV and 200 mA with a scan rate of 1 s per step (0.05°).

578

579

580

581

582

583

Mechanical properties. The mechanical properties of the prepared membranes were tested using a universal testing machine (UTM, AGS-J 500 N, Shimadzu, Kyoto, Japan) at a stretching rate of 10 mm/min. TGA was performed using a Q50 apparatus (TA Instruments). The thermal stabilities of the PBI membranes and the CeHP sheet were examined via TGA (Q500 Thermobalance, TA Instruments, USA). Under ambient conditions, 10 mg of the PBI membranes and the CeHP sheet were heated at a rate of 10 °C/min to 800 °C

584

585

586

587

588

***In-situ* high-temperature Raman spectroscopy.** Raman measurements were performed with a Renishaw inVia Raman microscope. The Raman microscope was equipped with a red laser diode, for which $\lambda = 785$ nm and output power = 50 mW. The laser power was optimized to avoid any photobleaching or damages to the membranes by the excitation energy. The samples were kept in a dry chamber during data acquisition to prevent any interaction between the air humidity and

589 the phosphoric acid. Spectra were collected in the range of 700-2000 cm^{-1} , and the spectral
590 resolution was 9 cm^{-1} .

591 **High-temperature solid-state NMR spectroscopy.** ^1H and ^{31}P MAS NMR spectroscopy was
592 performed using a Bruker DSX-500 spectrometer and a 4 mm Bruker MAS NMR probe. First,
593 the PEM was loaded into a 4 mm rotor, which was evacuated at 130 $^\circ\text{C}$ for 1 h. Then, it was
594 purged with Ar gas and closed with a tight-fitting Vespel cap for MAS at room temperature or a
595 variable temperature for *in-situ* NMR measurements. The samples were spun at 8 kHz under a
596 dry N_2 atmosphere. All spectra were reported in ppm using TMS and H_3PO_4 as standard
597 references for ^1H and ^{31}P NMR spectroscopy, respectively, calibrated at 0 ppm.

598 **Acid doping levels measurement.** The PA-doping level of PEMs was determined by the weight
599 analysis method through the following procedure. PEM samples measuring 3.8 cm x 3.8 cm were
600 weighed, the water content of PEM samples were measured using moisture analyzers (MA.R
601 series, RADWAG); the samples were immersed in water for 3 days and dried in a vacuum plate
602 at 130 $^\circ\text{C}$ for 8 h and weighed again. The doping level was calculated from the following equation:

$$603 \quad \text{Doping level} = \frac{\text{PA mole}}{\text{PBI PRU mole}} = \frac{W_{\text{PA}}/M_{\text{PA}}}{W_{\text{polymer}}/M_{\text{polymer}}}$$

604 where W_{PA} (g) is the PA weight in the polymer, M_{PA} (g mol^{-1}) is the molecular weight of the PA
605 in the polymer, W_{polymer} (g) is the dry polymer weight, and M_{polymer} (g mol^{-1}) is the molecular
606 weight of the polymer repeat unit.

607 The weight of PA (W_{PA}) was calculated from the following equation:

$$608 \quad W_{\text{PA}} = W_{\text{polymer+PA}} - W_{\text{polymer}}$$

609 where $W_{\text{PBI+PA}}$ (g) is the weight of the polymer from which moisture has been removed.

610 **MEA fabrication.** MEAs were prepared from catalyst inks containing Pt/C catalysts (TANAKA,
611 Pt 46.2 wt.%) and a PTFE solution (Sigma Aldrich, 60 wt.% dispersion in H₂O) as the binder, in
612 addition to isopropyl alcohol (IPA) and deionized water (DIW). The catalyst ink composition
613 was 4.3 wt% Pt/C, 2.3 wt% PTFE solution, 66 wt% IPA, and 26 wt% DIW. The catalyst slurry
614 was then auto-spray coated onto the gas diffusion layer (38BC, SGL). Subsequently, heat
615 treatment was performed at 350 °C for 5 min under an argon environment. The catalyst-coated
616 GDLs (Pt 1.5 mg cm⁻²) were used as anodes, and BASF commercial electrodes (Pt 1.0 mg cm⁻²)
617 were used as cathodes. In the experiment, to see the effect of the membrane, a BASF commercial
618 electrode (Pt 1.0 mg cm⁻²) was used for the anode. Prior to assembly, the PEMs were heated at
619 130 °C for 15 minutes. The MEAs were assembled in the single-cell by placing the PA-doped
620 PBI membrane between the anode and the cathode using gaskets. Hot pressing of the MEA was
621 not carried out. The active area of each MEA was 7.84 cm².

622 **Fuel cell characterization.** H₂/O₂ (or air) fuel cell performance of the MEAs was measured
623 using a fuel cell test station (CNL, Seoul, Korea). The polarization curves of the MEAs were
624 obtained at temperatures ranging from 150 to 250 °C. H₂ and O₂ (or air) were supplied at a rate
625 of 400 and 800 (or 1200) sccm, respectively. The same conditions were used for electrochemical
626 impedance spectroscopy (EIS), performed at an amplitude of 10 mA and frequencies of 10 kHz
627 to 1 Hz in the cell voltage range of 0.85–0.6 V. For long-term stability tests, the voltage at a
628 constant current density (0.2 A·cm⁻² or 0.5 A·cm⁻²) was measured every minute. The CO tolerance
629 test was performed using 25 cm² fuel cell hardware by feeding 10 wt% CO in the H₂ stream. The
630 voltage at a constant current density of 0.2 A·cm⁻² was measured at 250 °C as a function of time.

631 **Fuel cell operation with LHC dehydrogenation.** To prepare a H₂-rich LHC (LHC+),
632 methanol (Samchun chemicals) was mixed with deionized water to obtain a S/C ratio of 1:1.
633 N-ethylcarbazole (NEC, Sigma Aldrich) was hydrogenated to perhydro N-ethylcarbazole (12-
634 NEC, Sigma Aldrich) for the dehydrogenation experiments. For the catalyst, commercial Cu-
635 Ni on alumina (MDC-3, Süd-Chemie) was used for methanol reforming, and Pd/C (Riogen)
636 was used for NEC dehydrogenation. The flowrates of the gases, N₂ for purging and H₂ for
637 catalyst reduction or the direct operation of PEMFCs, were controlled using electrical mass
638 flow controllers (MFCs, F-201C, Bronkhorst, High-Tech). A high-pressure liquid
639 chromatography pump (Series II Legacy HPLC pump, TELEDYNI SSI) was used to feed the
640 methanol or 12-NEC into the reactor. The reactor was heated by electrical heaters with
641 temperatures being controlled. After the reaction, the product gas was fed to the liquid-gas
642 separator. The flowrates of the produced gas mixtures containing H₂ were measured using film
643 flow meters (SF-1U, Horiba, Japan). For power generation experiments, the performances of
644 the fuel cell using H₂ from a gas cylinder and that using H₂ produced by the reactor were
645 evaluated and compared. The product gas was fed either to the GC (Agilent 7890, Agilent) for
646 compositional analysis or to the PEMFC for the power generation experiments.

647

648 **Data availability**

649 Data supporting the plots within this paper and other findings of this study are available from
650 the corresponding author upon reasonable request.

651

652 **Acknowledgements:** This work was supported by the project “KIST Institutional Program”
653 from the Korea Institute of Science and Technology and supported by the Industrial Strategic
654 Technology Development Program (20011712) funded by the Ministry of Trade, Industry &

655 Energy (MOTIE, Korea).

656

657 **Author contributions:** † These authors contributed equally to this work. S.Y. Lee and N.-W.
658 Nam developed the intellectual concept and supervised this research; H.-J. Kim guided the
659 work; S. Lee., Y. Jo., and S.-J. Hwang, S. Y. Lee and N.-W. Nam wrote the manuscript. S. L.,
660 Y. J., and Y. K. designed all the experiments. S. Lee prepared the SAN-CeHP PBI polymer and
661 performed the MEA fabrication and testing experiments of fuel cells. S. Lee measured all
662 membrane properties and analyzed all experimental data. Y. Park prepared the dehydrogenation
663 of hydrogenated N-ethylcarbazole. Y. Jo and Y. Kim measured the performance of HT-PEMFC
664 integrated with H₂ extraction unit. T. K. Lee conducted a Figure 1 schematic diagram. S. -J.
665 Hwang conducted solid NMR analysis and analyzed NMR data. All the authors discussed the
666 results and commented on the draft.

667

668 **Competing interests:** The authors declare no competing financial interests.

669

670 **Supplementary Information** is available for this paper.

671 **Additional information:** Correspondence and requests for materials should be addressed to S.
672 Y. L. (sylee5406@kist. re.kr), S. W. N. (swn@kist.re.kr) or H.-J. K. (hjkim25@kist.re.kr).

673 Reprints and permissions information is available at www.nature.com/reprints

674

675

676 **Extended Data Legends**

677

678 **Extended Data Figure 1 | Cerium hydrogen phosphate (CeHP). a, CeHP image. b, SEM**

679 image of CeHP surface. **c**, XRD profiles of CeHP at different temperatures: (a) initial product,
680 (b) heated at 130 °C, and (c) heated at 300 °C. **d**, Thermogravimetric analysis (TGA) profile
681 of CeHP.

682

683 **Extended Data Figure 2 | Solvation behavior of CeHP ionomer mixed with concentrated**

684 **H₃PO₄. a–d**, Solid-state ³¹P MAS NMR spectra of CeHP ionomer: (a) CeHP ionomer mixed
685 with concentrated H₃PO₄, (b) after heating at 250 °C, (c) mixed for different times, and (d)
686 mixed at different temperatures.

687

688 **Extended Data Figure 3 | Fuel cell test of SAN-CeHP-PBI. a-b**, Scanning electron

689 microscope images of PA-doped SAN-CeHP-PBI composite membrane after 100h at (a) 150°C
690 and (b) 250 °C of fuel cell testing. **c-d**, Fuel cell performance, *i*-V curve with Pt/C (1.5 mg_{Pt}·cm⁻
691 ²) and the PA-doped SAN-CeHP-PBI composite membrane (*t* = 110μm) using (c) H₂/O₂ and
692 (d) H₂/Air at 150-250°C under 3 bar without humidification.

693

694 **Extended Data Figure 4 | Proton conductivity mechanisms. a–b**, (a) *p*-PBI; Grotthus-type

695 hopping mechanism via benzimidazole ring between H₃PO₄ molecules at below 180 °C. (b)
696 SAN-CeHP-PBI composite membrane; a surface/interfacial conduction via proton transfer
697 between benzimidazole ring–cerium hydrogen phosphate and cerium hydrogen phosphate
698 molecules at elevated high temperature of over 200 °C.

699

700 **Extended Data Figure 5 | Structural change of PA-doped PBI membranes according to**

701 **temperature. a**, Membrane images of the *p*-PBI membrane, CeHP-PBI composite membrane,
702 and SAN-CeHP-PBI composite membranes. **b-c**, Scanning electron microscope images of (b)

703 before and (c) after 100h of heating at 250 °C for all three samples. **d**, EDX mapping images
704 after 100h of heating at 250 °C of Ce element for all three samples. **e–g**, Raman spectra of *p*-
705 PBI membrane, CeHP-PBI composite membrane, and SAN-CeHP-PBI composite membrane
706 at (e) 30 °C and (f) after de-doped at 30 °C.

707

708 **Extended Data Figure 6 | Mechanical stability property of PBI membranes. a-b**, Tensile
709 property comparison (a) PA-doped and (b) De-doped among *p*-PBI membrane, CeHP-PBI
710 composite membrane, and SAN-CeHP-PBI composite membrane

711

712 **Extended Data Figure 7 | Acidic proton mobility of the de-doped PBI membranes. a**, NMR
713 quantitation of total ³¹P signal among H₃PO₄, HPO₄, PO₄ phases normalized by weight of all
714 three samples; filled symbol; PA-doped; unfilled: De-doped. **b**, XRD profiles of De-doped *p*-
715 PBI membrane, CeHP-PBI composite membrane, and SAN-CeHP-PBI composite membrane.
716 **c**, Membrane images, scanning electron microscope images, and EDX mapping images of Ce
717 element, the De-doped of *p*-PBI membrane, CeHP-PBI composite membrane, and SAN-CeHP-
718 PBI composite membrane. **d-f**, ³¹P solid-state MAS NMR spectra of De-doped (d) *p*-PBI
719 membrane, (e) CeHP-PBI composite membrane, and (f) SAN-CeHP-PBI composite membrane
720 shown for all four samples as T rises. **h-j**, ¹H solid-state MAS NMR spectra of De-doped (h)
721 *p*-PBI membrane, (g) CeHP-PBI composite membrane, and (i) SAN-CeHP-PBI composite
722 membrane and CeHP powder shown for all four samples as temperature rises.

723

724 **Extended Data Figure 8 | Reversible SAN-CeHP-PBI. a-b**, *i-V* curve with Pt/C (1.5 mg_{Pt}·cm⁻²)
725 ²) and (a) PA-doped SAN-CeHP-PBI composite membrane (*t* = 110 μm) and (b) Re-PA-doped
726 SAN-CeHP-PBI composite membrane (*t* = 120 μm), soaked in water for 3 days and then

727 immersed in 85% PA for 1 day at 30 °C, using H₂/air with no backpressure at 150–250 °C. **c**,
728 Long-term stability of Re-PA-doped SAN-CeHP-PBI composite membrane ($t = 120 \mu\text{m}$) with
729 Pt/C ($1.5 \text{ mg}_{\text{Pt}} \cdot \text{cm}^{-2}$). The fuel cells were tested at a constant current density of $0.2 \text{ A} \cdot \text{cm}^{-2}$ at
730 250 °C in H₂/air under anhydrous conditions.

731

732 **Extended Data Figure 9 | Effect of cerium content on the fuel cell performance of**
733 **composite membranes. a-c**, H₂/Air fuel cell performance, *i*-V curve with the various PA-
734 doped SAN-CeHP-PBI composite membranes with 15, 35, 70 and 90 wt% Cerium precursor
735 ($t = 110 \mu\text{m}$), with Pt/C ($2.0 \text{ mg}_{\text{Pt}} \cdot \text{cm}^{-2}$, BASF commercial electrode) no backpressure at (a) 150,
736 (b) 200 and (c) 250 °C.

737

738 **Extended Data Figure 10 | Electrochemical analysis of 35wt% SAN-CeHP-PBI composite**
739 **membranes a-b**, Electrochemical impedance spectroscopy of PA-doped 35wt% SAN-CeHP-
740 PBI composite membranes before and after 7000min operation at a current density of $0.2 \text{ A} \cdot \text{cm}^{-2}$
741 and measured (a) 0.85V and (b) 0.6V

742

743 **Extended Data Figure 11 | Conceptual design of an integrated HT-PEMFC for power**
744 **generation systems. a**, Properties of representative hydrogen carriers applicable to the on-
745 board hydrogen storage system. Thermodynamic reaction temperature required for > 99%
746 conversion with a reported range of kinetic reaction temperature range for > 60% conversion
747 with varying catalysts in the literature and theoretical reaction enthalpy of hydrogen extraction
748 reaction of the candidates with a proportion of extracted hydrogen required to provide the
749 theoretical reaction heat. **b**, Theoretical energy efficiency comparison with low, high-
750 temperature polymer electrolyte membrane fuel cells and direct liquid hydrogen carrier fuel

751 cells as a source of liquid hydrogen carrier for electricity generation from fuel cells. **c-d**, (c)
752 Schematic diagram, and (d) image of the experimental system LHC (methanol and N-
753 ethylcarbazole) reforming or dehydrogenation in conjunction with a unit cell using PA-doped
754 35wt% SAN-CeHP-PBI composite membrane ($t = 110 \mu\text{m}$).

755

756 **Extended Data Table 1 | Cell Performance of comparison of different types of fuel cells as**
757 **reported in the literature.**

758

759 **Extended Data Table 2 | Assignment of Raman signals of PA-doped and de-doped SAN-**
760 **CeHP-PBI**

761

762 **Extended Data Table 3 | Properties of representative hydrogen carriers applicable to on-**
763 **board hydrogen storage system.** Thermodynamic reaction temperatures required for $> 99\%$
764 and $> 95\%$ of the degree of dehydrogenation (DoDH) are estimated by either calculation or
765 from the literature. Literature data on kinetic reaction temperatures for over 60% conversion of
766 the reactant to hydrogen is listed, and the range denotes different DoDH with different catalysts.
767 Moreover, the heat of reaction and reaction stoichiometry are listed.

Supplementary Files

This is a list of supplementary files associated with this preprint. Click to download.

- [Supplementaryinformationfinal.pdf](#)
- [GXMyDriveJGJGManuscripts2021NENERGY21081496Supplementaryinformationfinalrevised.pdf](#)
- [ExtendedDataFiguresfinal.docx](#)
- [ExtendedDataTablefinal.docx](#)